Mitotic waves in the early embryogenesis of *Drosophila*: Bistability traded for speed

Massimo Vergassola[a,1], Victoria E. Deneke[b], and Stefano Di Talia[b,1]

[a]Department of Physics, University of California, San Diego, La Jolla, CA 92093; and [b]Department of Cell Biology, Duke University Medical Center, Durham, NC 27710

Edited by Boris I. Shraiman, University of California, Santa Barbara, CA, and approved January 17, 2018 (received for review August 22, 2017)

Early embryogenesis of most metazoans is characterized by rapid and synchronous cleavage divisions. Chemical waves of Cdk1 activity were previously shown to spread across *Drosophila* embryos, and the underlying molecular processes were dissected. Here, we present the theory of the physical mechanisms that control Cdk1 waves in *Drosophila*. The in vivo dynamics of Cdk1 are captured by a transiently bistable reaction–diffusion model, where time-dependent reaction terms account for the growing level of cyclins and Cdk1 activation across the cell cycle. We identify two distinct regimes. The first one is observed in mutants of the mitotic switch. There, waves are triggered by the classical mechanism of a stable state invading a metastable one. Conversely, waves in wild type reflect a transient phase that preserves the Cdk1 spatial gradients while the overall level of Cdk1 activity is swept upward by the time-dependent reaction terms. This unique mechanism generates a wave-like spreading that differs from bistable waves for its dependence on dynamic parameters and its faster speed. Namely, the speed of "sweep" waves strikingly decreases as the strength of the reaction terms increases and scales as the powers 3/4, −1/2, and 7/12 of Cdk1 molecular diffusivity, noise amplitude, and rate of increase of Cdk1 activity in the cell-cycle S phase, respectively. Theoretical predictions are supported by numerical simulations and experiments that couple quantitative measurements of Cdk1 activity and genetic perturbations of the accumulation rate of cyclins. Finally, our analysis bears upon the inhibition required to suppress Cdk1 waves at the cell-cycle pause for the maternal-to-zygotic transition.

waves | bistability | cell cycle | *Drosophila* | noise

Early embryogenesis in insects and amphibians unfolds outside of the mother, which arguably imposes selective pressure for speed to limit the risks of predation and parasitoids (1). After fertilization, a series of swift and synchronous cleavage divisions leads to coordinated increase in the amount of DNA and number of cells, before activation of zygotic gene expression and morphogenesis (2).

Waves are observed in biological systems that range from axonal action potentials, to calcium waves, and to mitotic waves in development (3). In physics, traveling waves are observed when a stable phase of matter invades a metastable one, e.g., in supercooled liquids (see ref. 4 for review). The classical mechanism for traveling waves is the coupling of reactions and diffusion in time-independent bistable systems (3, 4). Systematic theory determines the speed of bistable waves (5), captures the weak dependency on the noise level in the dynamics (6–9), and yields analytical solutions in special cases (5, 10, 11).

The above bistable mechanism was proposed for the synchronization of the cell cycles across hundreds of micrometers spanned by metazoan embryos (12–14). For a *Xenopus* extract system that carries out cell cycles in vitro, mitosis spreads at about 60 μm/min, comparable to surface contraction waves in the cell cortex that precede cytokinesis. Control of the speed is important as slow waves might produce chaotic desynchronization (14, 15), while fast waves might generate mechanical instabilities that disrupt nuclear arrangement (16).

During the early stages of embryogenesis, nuclei in the syncytial *Drosophila* embryo undergo 13 rounds of cleavage divisions before pausing the cell cycle at the maternal-to-zygotic transition (17–19). Cell cycles last only 8 min at the earliest stages and progressively slow down to 18 min for the last cycle 13 (18, 19). Completion of mitoses advances (see Fig. 1*A*) at speeds of a few hundred micrometers per minute, which span the entire embryo in 1–2 min. The speed systematically slows down (20) over the last cycles of the above 13 rounds (17–19). Confocal imaging of a Förster resonance energy transfer (FRET) biosensor was recently shown (21) to yield precise space–time measurements of the activity of Cdk1, the cell-cycle master regulator (Fig. 1*B*). The technique allowed the authors to demonstrate the chemical nature of the wave-like spreading of Cdk1 (21). Surgical ligation experiments showed that Cdk1 waves spread during the S phase of the cell cycle and control the subsequent mitotic waves (21). The increased activation of the DNA replication checkpoint kinase Chk1 and the consequent slowdown of the S phase explain the deceleration of the waves in the final cycles of division.

Mathematical models for developmental waves are based on reaction–diffusion systems that describe the feedback loops between Cdk1, the phosphatases Cdc25, and the kinase Wee1 (22, 23). Models for *Xenopus* (12) and *Drosophila* (21) have similar structure, except for the inclusion of Chk1 to account for the slowdown of *Drosophila* waves with the cycles. Models feature substantial time dependency, which is due to the variable levels of cyclins and Cdk1 activation across each cell cycle. This constitutes a notable difference with respect to the time-independent standard models for bistable waves (3, 4).

Significance

Early embryogenesis of most metazoans features rapid and synchronous cell divisions. In *Drosophila* embryos, traveling waves of activity of Cdk1, the master regulator of the cell cycle, are responsible for the synchronization of the cell cycle. Here, we elucidate the spreading of Cdk1 waves by demonstrating a unique physical mechanism for the generation of waves in biological systems. The mechanism hinges on time-dependent effects in a reaction–diffusion system, namely the fact that they can sweep the overall level of the Cdk1 field upward, while preserving its spatial gradients. The resulting waves are faster than those triggered by the invasion of a metastable state by a stable state. Theoretical predictions are confirmed experimentally by direct live imaging of Cdk1 activity.

Author contributions: M.V. and S.D.T. designed research; M.V., V.E.D., and S.D.T. performed research; M.V., V.E.D., and S.D.T. contributed new reagents/analytic tools; M.V., V.E.D., and S.D.T. analyzed data; and M.V. and S.D.T. wrote the paper.

The authors declare no conflict of interest.

This article is a PNAS Direct Submission.

[1]To whom correspondence may be addressed. Email: massimo@physics.ucsd.edu or stefano.ditalia@duke.edu.

This article contains supporting information online at www.pnas.org/lookup/suppl/doi:10.1073/pnas.1714873115/-/DCSupplemental.

Published online February 15, 2018.

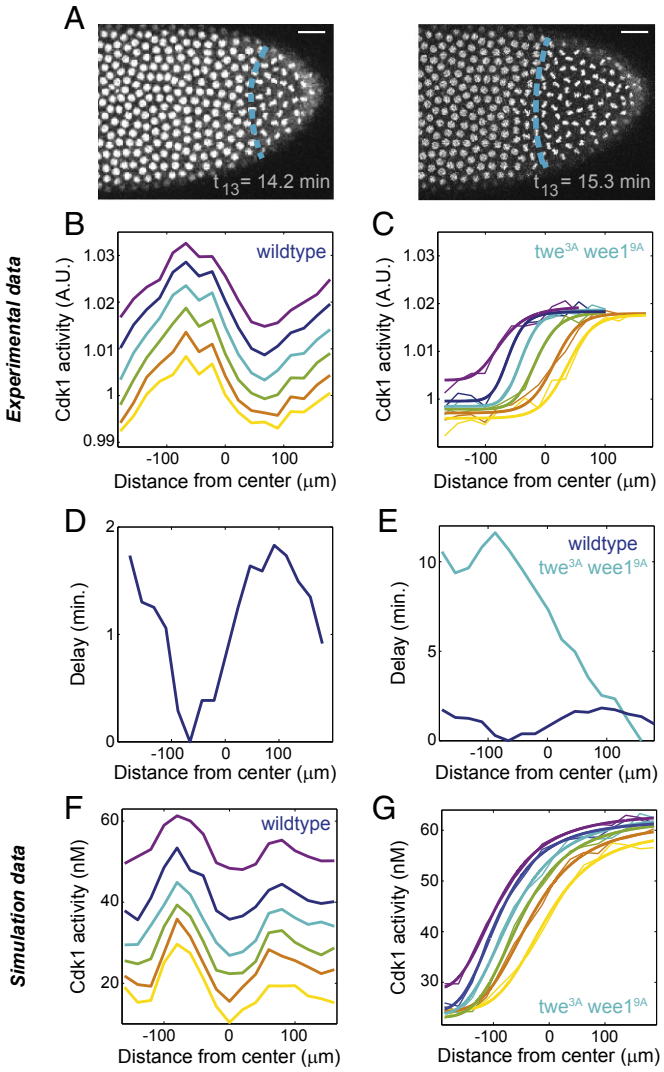

Fig. 1. Spatiotemporal patterns of Cdk1 activity differ in wild type and mutants of the mitotic switch. (*A*) Confocal images of embryos expressing His2Av-mRFP allow us to visualize the wave-like spreading of mitotic events across the embryo. (Scale bar: 10 μm.) *B* and *C* show the spatial profile of Cdk1 activity measured experimentally by using a FRET-based biosensor (curves are separated by 60 s and 90 s, respectively). (*B*) In the wild type, the Cdk1 activity grows synchronously, with minor distortions of the gradients. (*C*) In the mutant lacking the mitotic switch feedbacks (see Fig. S1 for details), a sharp front propagates across the embryo. (*D*) In the wild type, the Cdk1 activity crosses a given threshold level of activity with delays that vary piecewise linearly in space, as for traveling waves. (*E*) Wild-type waves are faster than in the mutant in *C*, as shown by the time delays in threshold crossings. (*F* and *G*) The reaction–diffusion model Eq. **1** of Cdk1 activity recapitulates experimental observations.

Our goal here is to develop the theory of waves in time-dependent reaction–diffusion models and apply it to *Drosophila* embryos. A first sense of its biological relevance is grasped by the time evolution of experimental Cdk1 profiles shown in Fig. 1 *B* and *C*. Profiles in wild-type embryos (Fig. 1*B*) differ from a bistable front, which is visible in Fig. 1*C* (obtained for mutants of the mitotic switch, below). In particular, the levels of activity at the left/right ends in Fig. 1*C* (which correspond to the metastable/stable points of the corresponding bistable system) are roughly unchanged in time while a front progresses. Conversely, the wild-type profiles do not show any sign of invasion by a stable phase of a metastable one. We will substantiate these visual hints and trace their origin back to the strength of time-dependent effects in the dynamics.

Qualitative aspects of Fig. 1 *B* and *C* are also observed in the general setting of reaction–diffusion systems. Below, we revisit (quartic) bistable potentials discussed in ref. 5, by adding a time-dependent component to the potential. Two regimes will emerge: (*i*) a fast regime, where time-dependent effects are strong, and the profiles of the field are as in Fig. 1*B*, and (*ii*) a quasi-adiabatic regime, where time dependencies are slow and bistable waves as in Fig. 1*C* are observed, which conform to the analytical solution for the static case (10, 11).

A major consequence of the dynamics underlying the above visual differences is that the wave-like spreading of Cdk1 in wild-type *Drosophila* embryos is generated by a unique physical mechanism that we dubbed "sweep waves." The reason is that it hinges on the upward sweeping of the Cdk1 activity field, i.e., an overall increase of its level, with minor distortions of its spatial gradients, as observed in Fig. 1*B*. We use the above quartic potential problem (5) to theoretically determine speed and functional dependencies of sweep waves. We test our predictions by numerical simulations and experiments on wild-type and mutant *Drosophila* embryos. We conclude by discussing consequences for the suppression of Cdk1 waves at the maternal-to-zygotic transition.

Results

Phenomenological Observations. We first present experimental results and their counterparts in numerical simulations of reaction–diffusion models. Data, namely the space–time profiles of the fields and the fact that bistable waves are too slow to explain experimental and numerical observations, provide the motivation for the theory in the following section.

Two distinct regimes are found experimentally for Cdk1 waves in* Drosophila *embryos. Fig. 1 *B* and *C* shows the spatial profile of Cdk1 activity over a cell cycle, measured by using the biosensor (21) mentioned in the Introduction. The mutant in Fig. 1*C* is obtained by altering the positive feedback mechanism that sharpens mitotic entry (see *Materials and Methods* and Fig. S1 for details). Fig. 1*D* shows the times for the Cdk1 activity at a given location to cross prescribed threshold levels vs. the position in space. While not quite straight lines (as would be for an exact wave), regions that vary in space roughly in a piecewise-linear manner are clearly visible. Local linear fits allow us to reliably extract wave speeds, which are faster in the wild type than in the mutant (Fig. 1*E*).

As already mentioned, Fig. 1*C* is consistent with the profiles expected for a bistable wave, with the upper (stable) level of Cdk1 activity invading the (metastable) lower level (3, 4, 12). No such evidence is visible for the wild-type profile in Fig. 1*B*.

Both Experimental Regimes Are Captured by Reaction–Diffusion Models. Regulatory interactions among Cdk1, the phosphatases Cdc25, the kinase Wee1, and the checkpoint kinase Chk1 are schematically shown in Fig. 2*A*. As in ref. 12, the effects of the feedback loops are incorporated by phenomenological reaction terms, rather than by equations for each chemical species. The resulting equation for the Cdk1 activity $a(x,t)$ reads

$$\partial_t a(x,t) = D\nabla^2 a(x,t) + G(a,t) + \eta(x,t), \qquad [1]$$

where $G(a,t) \equiv G_0\,[\alpha + r_+(a)\,(c(t)-a) - r_-(a)\,a]$ is the reaction term that accounts for the feedback loops, viz. $r_+(a)$ and $r_-(a)$ are the phenomenological Hill functions that describe the regulation of Cdk1 activity by Cdc25, Wee1, and Chk1; detailed expressions are in *A Reaction–Diffusion Model for Cdk1 Waves*.

The synthesis term α recapitulates diverse molecular events that drive the cell cycle, e.g., synthesis of cyclins, inactivation of

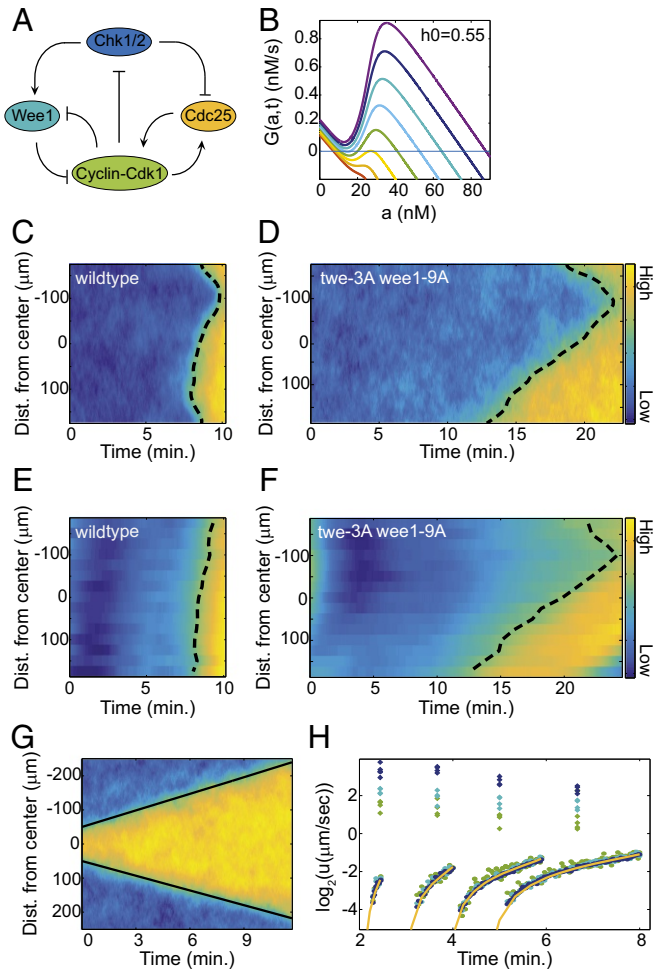

Fig. 2. Reaction–diffusion models of Cdk1 activity recapitulate experimental observations. (*A*) Scheme of the molecular interactions used in our reaction–diffusion model Eq. **1**. (*B*) The force field in the model for an initial Chk1 level $h_0 = 0.55$, which roughly corresponds to the cell cycle 13. The lowest curve corresponds to $t = 0$ and successive curves are separated by 2 min. (*C* and *D*) Heat map of the Cdk1 activity from simulations of our reaction–diffusion model ($h_0 = 0.55$ as in *B*) in wild type (*C*) and the mutant lacking the mitotic switch feedback (*D*). The dashed curves indicate the times at different spatial points for the Cdk1 activity to cross a threshold level roughly corresponding to metaphase. (*E* and *F*) Experimental heat maps of the Cdk1 activity for the cell cycle 13 of a wild-type (*E*) and a mutant (*F*) embryo. (*G*) Heat map of Cdk1 activity for a metastable potential frozen at the time $t = 6.5$ min ($h_0 = 0.55$). The bistable wave was obtained by poising the middle region close to the stable point of the force *G* in *B* and the rest of the space at its metastable point (with a sharp transition in between). (*H*) Solid lines show the speed of deterministic waves computed using the mechanical analogy in *Time-independent case*; circles show the speed of bistable waves measured in simulations of Eq. **1** with *G* frozen at different times and in the presence of different noise levels; diamonds show the speed in full simulations of Eq. **1** for different noise levels at a given h_0. The four groups of data are for $h_0 = 0.4, 0.45, 0.5, 0.55$.

mitotic phosphatases, and phosphorylation of Thr161 on Cdk1; $c(t)$ is the total amount of Cdk1 (active and inactive); η is the Langevin noise that accounts for the finite numbers of particles in chemical reactions (24). Profiles of $G(a, t)$ feature transient bistability for a range of Chk1 levels, with bistability more pronounced as Chk1 levels increase, i.e., for later developmental cycles (Fig. 2*B* and Fig. S2).

Eq. **1** captures several experimental observations. First, Fig. 1 *F* and *G* and Fig. S2*E* confirm the marked difference in the Cdk1 profiles for wild type and the mitotic switch mutant. Second, changes in the initial Chk1 activity reproduce the observed changes in the Cdk1 developmental dynamics (Fig. S2*C*): The increase in the Cdk1 activity during early stages (S phase) is reduced, while the rapid increase driving mitosis is unaltered (21). Third, the model shows wave-like patterns of Cdk1 activation in the wild type and the mutant (Fig. 2 *C*–*F*). Finally, the speed of the waves reduces as Chk1 increases (Fig. S2*D*) and reproduces the experimental data (Fig. S2*F*), as was already the case in ref. 21 (the two models differ in the numerical value of their parameters).

Bistable waves are slow. To further characterize the waves in Fig. 1, we used the mechanical analogy in refs. 4 and 5 (*Time-independent case* section) to compute the speed of bistable waves triggered by Eq. **1** statically, i.e., for the force G frozen at a fixed time during the window of bistability (Fig. 2*H*, circles). We validated those values by numerically simulating Eq. **1** with the corresponding frozen, time-independent forces G and measuring the speed of invasion by the stable phase of the metastable one (Fig. 2*G*). The maximum speed of bistable waves is reached for G frozen at the time when transient bistability is lost. However, even that maximum speed remains severalfold slower than waves in full simulations of Eq. **1**, i.e., including the time dependency of G (Fig. 2*H*, diamonds). Noise weakly affects bistable waves, as expected (4).

The Cdk1 wild-type dynamics over a single cell cycle feature three phases. Experimental data (and the above reaction–diffusion model) indicate that the dynamics of Cdk1 over a cell cycle feature three distinct phases, as sketched in Fig. 3.

At short times (phase I), Cdk1 levels are close to the low fixed point of the system (Fig. 3*A* and Figs. S4 and S5). As the slope at the fixed point decreases with time (Fig. 3*A*, *Inset*), the relaxation time and the correlation length of the field increase; i.e., relatively extended spatial regions become coupled by the combined action of diffusion and reactions (Fig. 3*B*). The embryo thereby separates in few blocks: Within each one of them the Cdk1 activity is strongly correlated and thus varies roughly linearly with well-defined spatial gradients.

Phase II takes place while values of the field are around the minimum of the force (Fig. 3*C* and Figs. S4 and S5). Functions vary little as their argument changes around a minimum, which allows us to treat the force as a constant that changes in time due to time dependencies. A constant force preserves the spatial gradients of the field, which is the mechanism leading to the upward sweeping of the profiles in Fig. 3*D* and Figs. S4 and S5. It is intuitive [and confirmed in *Synchronous Growth (Phase II)*] that spatial points along a linear gradient that is swept upward will cross a threshold level at times that vary linearly in space, as for a wave. This is the crux of the sweep wave mechanism discussed below.

Finally, during the third phase (Fig. 3*E* and Figs. S4 and S5), the field grows toward the only remaining fixed point. For the developmental case, the growth to the fixed point lasts minutes, and mitosis is completed before reaching it (Fig. S7*A*). That is the reason why phase III is the last period of interest here. Forces during phase III take relatively high values, the effect of their additive time-varying component is minor, and their nonlinear component plays the major role. As shown in *Autonomous Growth (Phase III)*, the resulting autonomous growth implies that delays are conserved; i.e., phase III conserves on average the differences among the times for different spatial points to pass prescribed threshold levels of the field, as in Fig. 3*F*, *Inset*.

Theory of Waves in Time-Dependent Reaction–Diffusion Systems. To understand the nature of the developmental waves in wild-type *Drosophila* and the three above phases, we analyze the general, time-dependent reaction–diffusion equation

$$\partial_t \phi(x,t) = D\nabla^2\phi(x,t) + F(\phi,t) + \sqrt{2\nu}\,\eta(x,t), \qquad [2]$$

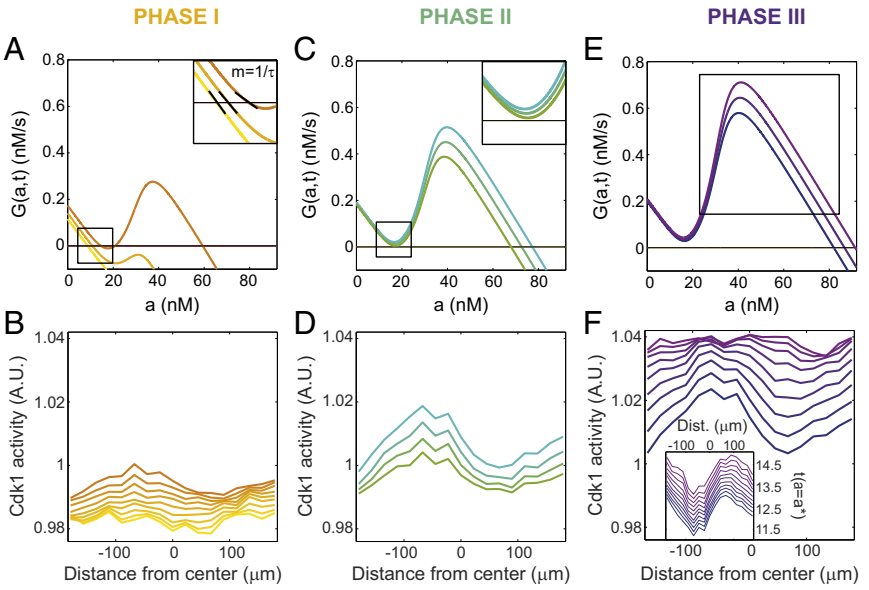

Fig. 3. The dynamics of Cdk1 over a single cell cycle display three distinct phases. (*A*) Force field for the Cdk1 model at early times. *Inset* shows the timescale of relaxation to the low steady state is the inverse of the negative slope of the force near the fixed point. (*B*) Temporal evolution of Cdk1 activity (from experimental data) as a function of space demonstrates the formation of gradients of increasing length. (*C*) Force field for the Cdk1 model at times around the loss of bistability. (*D*) Temporal evolution of Cdk1 activity (from experimental data) as a function of space demonstrates that gradients are swept up largely undeformed during this phase. (*E*) Force field for the Cdk1 model at times when the system is evolving rapidly toward the only remaining high stable state. (*F*) Temporal evolution of Cdk1 activity (from experimental data) as a function of space demonstrates that gradients change, yet the time delays among different spatial points to reach a given Cdk1 threshold of activity are conserved (*Inset*).

where ϕ is the field of interest, e.g., order parameter, enzymatic activity, etc.; D is the diffusivity; F is the reaction term; and η is Gaussian noise, with zero average and correlation $\langle \eta(x,t)\eta(x',t')\rangle = \delta(x-x')\delta(t-t')$. For development, $\phi(x,t)$ is the level of Cdk1 activity. The amplitude ν should a priori depend on ϕ (multiplicative noise). However, since for the Cdk1 model Eq. **1** the dependency is weak (Fig. S2*G*), we take ν constant (additive noise) for simplicity.

Revisiting quartic bistable potentials. We focus on the following cubic form for the time-dependent force F:

$$F(\phi,t) = -F_0\phi\left(\phi-\frac{1}{2}\right)(\phi-1)+\zeta(t). \qquad [3]$$

The rationale is that classical results (5, 10, 11), which provide the analytical solution for ζ fixed in time, will help us understand the time-dependent case $\zeta(t)=\beta t$ of interest here. The force F in Eq. **3** defines a potential V via $F \equiv -\frac{\partial V(\phi,t)}{\partial \phi}$. The force is bistable in the range $0 \le \zeta \le F^* \equiv F_0\sqrt{3}/36$ (Fig. 4*A*), where it has three zeros $\phi_0 \le \phi_1 < \phi_2$:

$$F(\phi,t) = -F_0(\phi-\phi_0)(\phi-\phi_1)(\phi-\phi_2). \qquad [4]$$

The corresponding potential (Fig. 4*B*) illustrates the metastability of ϕ_0 with respect to ϕ_2 and the unstable nature of ϕ_1. The curves of the fixed points ϕ_i vs. ζ are shown in Fig. 4*C*. The two small zeros coincide, $\phi_0=\phi_1=\phi^*=0.5-\sqrt{3}/6$ at the critical point $\zeta=F^*$. The derivative of F at ϕ_0 and ϕ_1, as well as their distance, vanishes $\propto \sqrt{F^*-\zeta}$ close to F^*.

Time-independent case. For values of ζ fixed in time (within the bistable range of the force), the combination of bistability and diffusion triggers bistable waves (4), as shown in Fig. 2*G*. The speed of the wave is obtained by inserting the ansatz $\phi(x-ut)=\phi(z)$ into the deterministic Eq. **2**:

$$D\frac{d^2\phi}{dz^2} = -u\frac{d\phi}{dz} - F(\phi,t). \qquad [5]$$

Interpreting the variable z as time, D plays the role of the mass of a particle moving into the force field $-F$, and u is the friction coefficient (5). The inversion $-F$ exchanges minima and maxima of the potential. The boundary conditions for the spreading of a

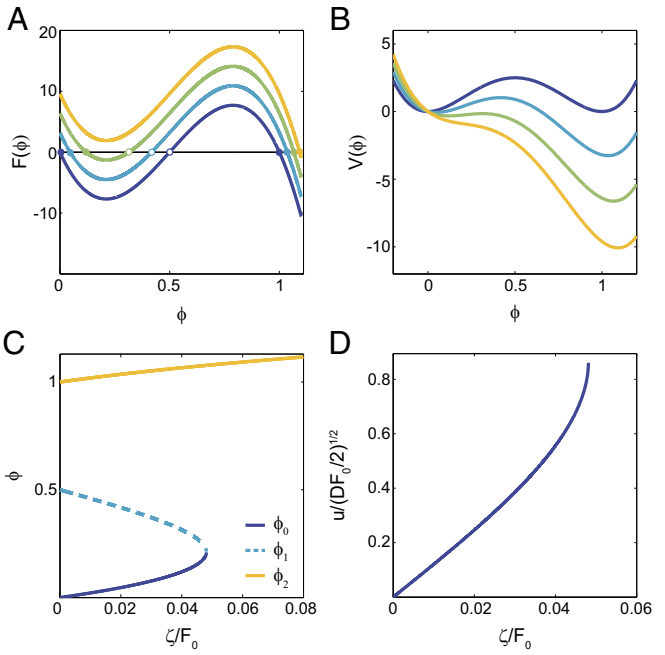

Fig. 4. A time-dependent theoretical model for chemical waves. (*A* and *B*) The force field (*A*) and the potential (*B*) in Eq. **3**, which display transient metastability (curves are shown for values of $\zeta/F_0 = 0$, 0.02, 0.04, and 0.06). (*C*) The values of the metastable ϕ_0, unstable ϕ_1, and stable ϕ_2 points as a function of ζ/F_0. (*D*) Dependency of the speed of bistable waves on the dynamic parameter ζ/F_0.

wave impose that the particle starts from the high peak of the bistable potential $-V$ and asymptotically lands on its low peak (Fig. S3). The speed of the bistable wave is the largest value of u that ensures this property (4). Dimensional arguments yield $u \propto \sqrt{DF_0}$ and $z \propto \sqrt{D/F_0}$, where F_0 is the amplitude of F.

No analytical solution to Eq. **5** is generally available and numerical methods must be used, as we did for Eq. **1** for the speeds in Fig. 2*H*. However, the cubic form Eq. **4** admits the analytical solution (5, 10, 11): $u = \sqrt{\frac{DF_0}{2}}\,(\phi_0 - 2\phi_1 + \phi_2)$. As ζ increases, ϕ_0 and ϕ_1 approach, yet ϕ_2 moves away (Fig. 4*C*). The resulting speed u increases (Fig. 4*D*) up to its maximum value $u^* \simeq 0.61\sqrt{DF_0}$ at the critical point $\zeta = F^*$.

Time-dependent case. The field ϕ in Eq. **2** initially starts from low values, like the Cdk1 field in development. As $\zeta(t) = \beta t$ in Eq. **3** increases, the lowest fixed point $\phi_0(\zeta)$ grows as in Fig. 4*C*. It is intuitive [and arguments in *Fluctuations and Gradients in the Quasi-Adiabatic Regime (Phase I)* confirm] that typical values of ϕ will be close to $\phi_0(\zeta)$, with noise-generated fluctuations that we analyze later. This approximation (quasi-adiabatic) holds as long as the potential around $\phi_0(\zeta)$ is steep enough; i.e., the relaxation to $\phi_0(\zeta)$ is rapid compared with changes of $\phi_0(\zeta)$ driven by β.

Two mechanisms compete as time progresses further:

i) Noise triggers the jump above the unstable point ϕ_1 (Fig. 4*B*) of a local region of the field ϕ. This nucleus grows rapidly up to ϕ_2 and spreads via bistable waves shown in Fig. 2*G*. This regime holds for small β.

ii) For larger β, deviations from the quasi-adiabatic approximation become important before the triggering of bistable waves. The dynamics are then strongly affected by time-dependent effects, as detailed below.

The analysis (*Materials and Methods*) of the first, slow regime shows that the speed of the bistable waves depends very weakly ($(-\log\beta)^{2/5}$) on the drive β, which is confirmed by numerical results in Fig. 5*A*. The dependence on other dynamic parameters is discussed in *Time-independent case*.

The second regime of fast drive is the one relevant to wild-type *Drosophila*. As in Fig. 3, the dynamics of Eq. **2** feature three phases (Fig. S5), which we proceed to investigate.

Fluctuations and gradients in the quasi-adiabatic regime (phase I). Far from the critical point ($\phi_0 = \phi_1 = \phi^*$ in Eq. **4**), fluctuations around ϕ_0 are captured by the linear approximation

$$\partial_t \phi(x,t) = D\nabla^2\phi(x,t) - \frac{\phi - \phi_0}{\tau} + \sqrt{2\nu}\,\eta(x,t). \qquad [6]$$

The relaxation rate $1/\tau = F_0\,(\phi_1 - \phi_0)(\phi_2 - \phi_0)$ is initially large, yet it vanishes as $\sqrt{F^* - \zeta}$, approaching the critical point. The correlation function $C(x) = \langle(\phi(x) - \phi_0)(\phi(0) - \phi_0)\rangle$ at the steady state is known (*Details on the Statistical Properties of the Adiabatic Regime*):

$$C(x) = C(0)\,e^{-\frac{|x|}{\lambda}}; \quad \lambda = \sqrt{D\tau}; \quad C(0) = \frac{\nu}{2}\sqrt{\frac{\tau}{D}}. \qquad [7]$$

It follows from Eq. **7** that ϕ at a given time is a Uhlenbeck-Ornstein process in space, i.e., Gaussian, with mean ϕ_0, variance $C(0)$, and exponential decay of correlations. The estimate of typical gradients is $g \sim \sqrt{C(0)}/\lambda$, i.e., the typical amplitude of the fluctuations divided by their characteristic length scale.

Note that the timescale τ in Eq. **7** is not the time t; i.e., the correlation length λ of the field generally differs from the diffusive length $\sqrt{Dt}$. Indeed, while τ is expected to increase with t, its time course depends on the shape of F, which reflects the joint role of diffusive and reactive terms in Eq. **6**.

As time progresses, the variation of the metastable state eventually becomes too rapid compared with the local relaxation time, nonadiabatic effects start to matter, and the growth of the field is delayed with respect to the metastable state (see *Materials and Methods* for details), as shown in Fig. 5 and discussed next.

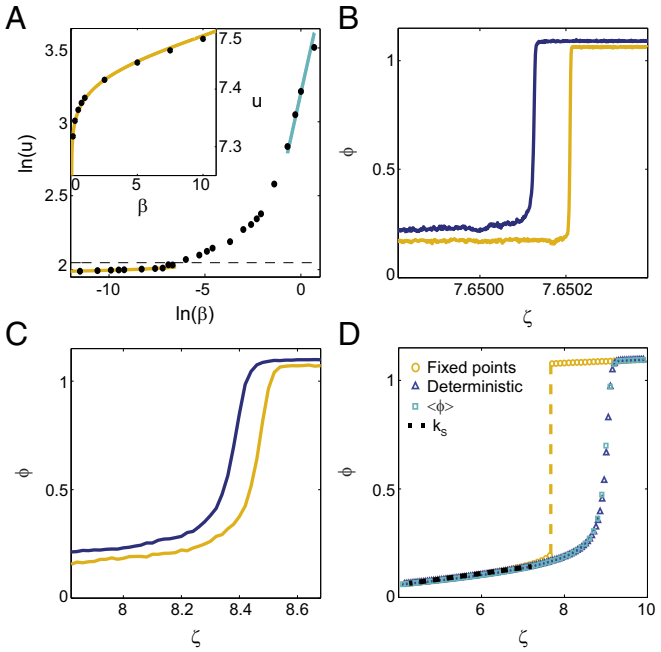

Fig. 5. Two different regimes are observed for the time-dependent reaction–diffusion Eq. **2**. (*A*) The wave speed u vs. the drive β in Eq. **3**. The yellow line is the fit with the prediction $(-\log\beta)^{2/5}$ in Eq. **13** for small β. The blue line is the fit with the prediction $\beta^{7/12}$ in Eq. **11** for the regime of fast drive. *A*, *Inset* shows a zoom-in of the $(-\log\beta)^{2/5}$ fit. (*B* and *C*) Maximum (blue) and minimum (yellow) of the field ϕ as a function of $\zeta = \beta t$ for $\beta = 10^{-4}$ and $\beta = 2$, respectively. The former illustrates bistable waves: While the wave spreads, the maximum is close to the upper stable point, while the rest of the field is still near the lower metastable point. Conversely, in the fast regime of large β, the field ϕ grows more uniformly across space, indicating the different nature of the dynamics. (*D*) The growth of the spatial average $\langle\phi\rangle$ vs. $\zeta = \beta t$ for $\beta = 5$ (yellow circles, the stable fixed points in Fig. 4*C*; light blue squares, $\langle\phi\rangle$; blue triangles, the numerical solution of Eq. **2** without noise). The dashed black linear fit defines the rate k_S of early growth (which corresponds to the S phase of the cell cycle, whence the notation).

Synchronous growth (phase II). Close to its minimum, the force F in Eq. **3** is approximated by its quadratic expansion

$$F \simeq \zeta - F^* + \gamma(\phi - \phi^*)^2, \qquad [8]$$

where $\zeta = \beta t$, $\gamma = F_0\sqrt{3}/2$, ϕ^*, and F^* are defined with Eq. **4**. The typical value $\zeta = \zeta^*(\beta)$ to reach the minimum ϕ^* differs from F^* due to nonadiabatic effects: Its scaling $\zeta^* - F^* \sim F_0\left(\beta/F_0^2\right)^{2/3}$ is predicted in *Materials and Methods* and confirmed in Fig. S6.

In a time window (below) around ζ^*/β, the dominant component in Eq. **8** is $\zeta - F^*$, and the quadratic term is negligible. It follows that the growth of ϕ is quadratic in time and uniform in space; i.e., gradients are conserved, as observed in Fig. 3. Integration of $d\phi/dt = \zeta - F^*$ (*Materials and Methods*) gives

$$\phi \simeq \phi^* + \frac{1}{\beta}\left[(\zeta^* - F^*)(\zeta - \zeta^*) + \frac{(\zeta - \zeta^*)^2}{2}\right]. \qquad [9]$$

By inserting Eq. **9** into Eq. **8**, we find that the quadratic term becomes comparable to $\zeta - F^*$ for amplitudes of $(\zeta - \zeta^*)/F_0$ and $(\phi - \phi^*)^2$ scaling as $\left(\beta/F_0^2\right)^{2/3}$, which is verified by numerical simulations in Fig. S6.

The mechanism of sweep waves. The consequence of the above synchronous growth is that the field $\phi(x,t)$, for positions x along a gradient g of ϕ, will reach a given threshold level $\overline{\Phi}$ at times that vary linearly in space, as for a traveling wave. Indeed, let us introduce space into Eq. **9** and consider a region that varies linearly, $\phi^* - gx$ at $\zeta = \zeta^*$ (the origin in space is shifted to simplify notation). By using Eq. **9**, we can find the times for various points x to pass a threshold $\overline{\Phi} > \phi^*$. Defining $\overline{\zeta}_{\overline{\Phi}}$ as the value of ζ when the origin $x = 0$ reaches the threshold, and assuming that variations around that value are small, we obtain $\left(\overline{\zeta}_{\overline{\Phi}} - F^*\right)\left(\zeta - \overline{\zeta}_{\overline{\Phi}}\right) - \beta g x \simeq 0$. We conclude that time delays along a gradient g vary linearly in space, as is shown for the experimental data in Fig. 1 *B* and *D*. The speed u of the corresponding wave-like spreading is

$$u = \frac{\overline{\zeta}_{\overline{\Phi}} - F^*}{g}. \qquad [10]$$

Functional dependencies of the wave speed. To elucidate the dependencies of the speed u on the parameters D, ν, β, and F_0 that appear in Eq. **2**, we should determine the behavior of $\overline{\zeta}_{\overline{\Phi}} - F^*$ and g in Eq. **10**.

The first quantity follows from Eq. **9**: As $\phi - \phi^*$ increases, the quadratic term in Eq. **8** becomes important, the synchrony of growth is broken, and phase II concludes. That was shown above to occur at $\overline{\zeta}_{\overline{\Phi}} - F^* \sim F_0\left(\beta/F_0^2\right)^{2/3}$.

As for the gradients g, they are formed at the transition between phases I and II. Their scaling is derived in *Materials and Methods*: The amplitude $\phi^* - \phi \propto \beta^{1/3}$ at the transition gives the scaling of the relaxation time τ, which is then used in formulas analogous to Eq. **7** to yield the final scaling $g \sim \nu^{1/2}(\beta F_0)^{1/12} D^{-3/4}$.

By inserting the two previous relations into Eq. **10**, we conclude that the speed u of the sweep waves depends on the drive β, the molecular diffusivity D, the amplitudes of the noise ν, and the potential F_0, as

$$u \sim \frac{\beta^{\frac{7}{12}} D^{\frac{3}{4}}}{\nu^{\frac{1}{2}} F_0^{\frac{5}{12}}}. \qquad [11]$$

The inverse dependency on F_0 contrasts with the square-root dependency for bistable waves that was discussed in *Time-independent case*. The underlying reasons are that gradients at the denominator in Eq. **10** increase with F_0 and the extension of phase II at the numerator shrinks.

Autonomous growth (phase III). In phase III, spatial points along a gradient of the field ϕ grow by and large independently, and their rate of growth is roughly time independent; i.e., their growth is autonomous. Let us then consider the autonomous equation $d\phi/dt = F(\phi)$, where F is the force Eq. **3** at a fixed time during phase III. Integrating the previous equation between a level $\overline{\Phi}_1$ and a higher level $\overline{\Phi}_2$, we see that the time needed for that growth is fixed, i.e., does not depend on the time at which $\overline{\Phi}_1$ was reached. In the presence of noise, the above argument remains valid on average. We conclude that the delays set during phase II among the spatial points of the field ϕ are conserved on average during phase III, and they do not depend on the choice of the threshold $\overline{\Phi}$.

Implications for development follow by observing that phase I in Fig. 3 corresponds to the beginning/middle S phase of the cell cycle, phase II corresponds to the middle/end of the S phase, and phase III spans the various phases of mitosis. The conservation of the delays during phase III reflects the experimental observation that the waves at the entry into (and exit out of) mitosis are strongly correlated with the speed of the chemical Cdk1 wave generated during the S phase of the cell cycle (21).

Testing Theoretical Predictions. The goal of this section is the verification of the above theoretical predictions, namely Eqs. **10** and **11**, by using data from experiments and numerical simulations of the reaction–diffusion model Eq. **1**.

Numerical tests. We determined the speed u of the waves in numerical simulations of Eq. **1**, which recapitulates experimental results as shown in Fig. 2. Fig. 6 *A* and *B* demonstrates that the theoretical prediction Eq. **11** captures the increase of u as the amplitude of the noise decreases. Similarly, our prediction $D^{3/4}$ agrees with the scaling of u vs. the molecular diffusivity D in Fig. 6*C*. Finally, the inverse scaling with respect to the amplitude of the reaction terms in Eq. **11** is confirmed by Fig. 6*D*. Note that rescaling the amplitude of the reaction terms G_0 in Eq. **1** modifies also the rate β and the noise ν in Eq. **11**. The predicted scaling is then $-1/2 - 5/12 + 7/12 = -1/3$, as in Fig. 6*D*.

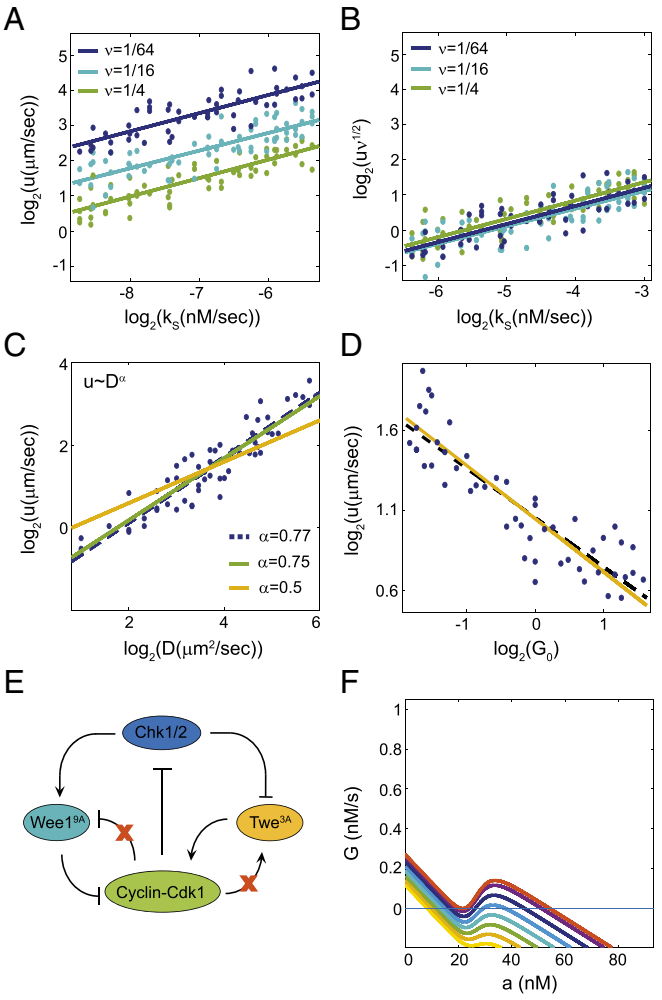

Fig. 6. Verification of theoretical predictions in the Cdk1 model Eq. **1**. *A* and *B* show the speed u of Cdk1 waves vs. the rate k_S of Cdk1 activation growth in the S phase, which is defined in Fig. 5*D*. Different values of the amplitude ν of the noise are shown in *A* and collapsed by the rescaling $u\nu^{1/2}$ in *B*, which supports the prediction Eq. **11**. (*C*) Plot of u vs. the Cdk1 diffusion coefficient D (dashed blue line, best fit; green line, the $D^{3/4}$ scaling predicted for sweep waves; yellow line, the $D^{1/2}$ scaling expected for bistable waves (*Time-independent case*). (*D*) Plot of u vs. G_0 defined in Eq. **1** (dashed black line, best fit; yellow line, the predicted scaling $G_0^{-1/3}$). (*E*) A scheme of the interactions in the mutant lacking the mitotic switch feedbacks. (*F*) Force field for the reaction–diffusion model of the mutant in *E*. The lowest curve corresponds to $t = 0$, and successive curves are separated by 3 min.

We can also use the model to rationalize the experimental observation that Cdk1 waves are slower in the mutant of the mitotic switch (Fig. 6*E* and Fig. S1). We compared the temporal dependency of $G(a,t)$ in Eq. **1** for the mutant (Fig. 6*F*) and the wild type (Fig. 2*A*): The metastable region is much more extended in the mutant (Fig. 6*F*), consistent with the bistable fronts in Fig. 1 *C* and *G*. Moreover, the experimental value $u \simeq 0.5$ μm/s is close to the speed in our simulations, $u = 0.47 \pm 0.04$, which is also consistent with the speed of bistable waves in the presence of noise (Fig. S7*D*).

Experimental tests. Our predictions in Eqs. **10** and **11** state that the speed of Cdk1 waves should (*i*) scale as the $2/3$ power of the rate of quadratic increase (which equals β) around the knee in the Cdk1 activation time profile (Fig. 5*D*) and (*ii*) be inversely proportional to the Cdk1 gradients. Experimental methods in ref. 21 allow us to measure those quantities (Fig. 7*A*–*C*) and thereby test our predictions. We decided to focus on the cell cycle 13, which is the slowest and thus constitutes the most stringent test for the sweep waves mechanism. We fitted experimental data in wild type and in *cyclin A* and *cyclin B* double-heterozygous mutants, which feature a reduced rate k_S of Cdk1 activity growth in the S phase of the cell cycle (Fig. 7*A* and *B*). The quadratic fit around the knee in Fig. 7*B* gives an estimate of β. We also estimated the spatial gradients of Cdk1 activity, as shown in Fig. 7*C*. The excellent agreement, in wild type and mutant alike, between the predicted $\beta^{2/3}/g$ and the experimental speeds is shown in Fig. 7*F*.

Additional support comes from the observation that the experimental speeds $u \propto \beta^{\gamma}$, with $\gamma = 0.6 \pm 0.1$ (Fig. 7*G*), which is consistent with our prediction $u \propto \beta^{7/12}$. In ref. 21, it was observed that $u \sim k_S^{1/2}$, where the slope k_S is the slope of Cdk1 activity's increase in the S phase. This empirical observation is explained here by our prediction $u \simeq \beta^{7/12}$ and the correlation between the slope k_S and the drive β (Fig. 7*H*).

A final piece of support comes from mutants where the rate k_S is modified. For bistable waves, this should have a relatively small effect (Eq. **13** in *Materials and Methods* and Fig. 5*A*). Conversely, a much stronger dependency is expected for sweep waves (Eq. **11** and Fig. 4*A*). In *cyclin A* and *cyclin B* double-heterozygous mutants, the S-phase slower activation of Cdk1 activity and the lengthening of the duration of the cell cycle (24 min vs. 18 min in the wild type) are likely due to the reduced synthesis rate of cyclins (Fig. 7*A*). Note that the cell cycle lengthening is significantly smaller than the naive twofold expectation, which would follow from the assumption of a fixed threshold on Cyclin A and/or Cyclin B for mitotic entry and the halved rate of accumulation of cyclins in the mutant. This observation is consistent with previous experiments (19). The average speed of Cdk1 waves in the mutant is significantly slower ($u = 0.9 \pm 0.1$ μm/s vs. the wild-type value $u = 1.8 \pm 0.1$ μm/s), which supports again that Cdk1 waves in *Drosophila* embryos are due to the sweep-waves mechanism described above.

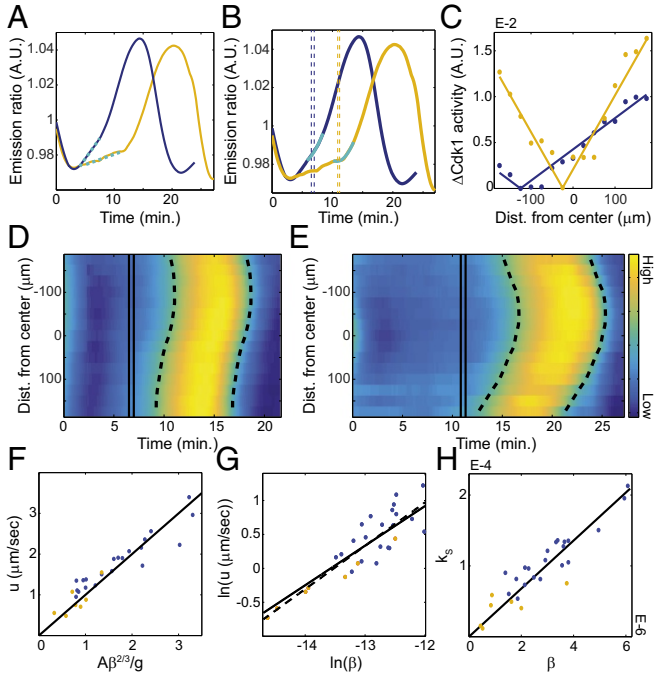

Fig. 7. Experimental data show that Cdk1 waves are sweep waves. (*A*) Emission ratio of the Cdk1 FRET biosensor as a function of time for a wild-type embryo (blue line) and a *cycA cycB* double-heterozygous mutant embryo (yellow line) for cell cycle 13. Linear fits (light blue lines) define the S-phase rate k_S of Cdk1 activity growth. (*B*) Emission ratio of the Cdk1 biosensor as in *A*. Green curves, quadratic fits to estimate the parameter β; dashed lines, the time frame used to estimate the gradients of Cdk1 activity. (*C*) The Cdk1 activity across the anterior–posterior axis, whence the gradient g is measured by fitting the data with two lines of the same slope. (*D* and *E*) Heat maps of the spatiotemporal Cdk1 activity for the wild type (*D*) and the *cycA cycB* double-heterozygous mutant (*E*). Black solid lines, the time frame used to estimate the gradients in Cdk1 activity; dashed lines, the times of mitotic entry and exit. (*F*) The Cdk1 waves' speed u vs. the prediction $u \propto \beta^{2/3}/g$ in Eq. **10**. The black line is the identity. (*G*) Scaling u vs. β (dashed line, best fit; solid line, theoretical prediction $u \sim \beta^{7/12}$). (*H*) The S-phase rate of Cdk1 growth k_S strongly correlates with the values of β fitted in *B*. The combination of results in *G* and *H* explains (noise makes 1/2 indistinguishable from 7/12) the empirical scaling $u \sim k_S^{1/2}$ previously reported in ref. 21.

Taming Waves at the Maternal-to-Zygotic Transition. A fundamental transition in the development of most metazoans is the switch from maternal to zygotic control at the midblastula transition (MBT) (25–27). The long pause in the cell cycle over the entire embryo, which is needed for completion of the MBT, requires that Cdk1 waves be suppressed. We combine our reaction–diffusion model with experiments to shed light on the mechanisms of control during the pause.

Specifically, the MBT is timed by the ratio of DNA to cytoplasm, which increases at each round of DNA replication until it reaches a threshold sufficient to trigger activation of zygotic gene expression and a cell cycle pause (27). This threshold-like response was revealed by experiments that altered embryonic DNA content by using compound chromosomes (28). Embryos with $\simeq$70% of the wild-type DNA content displayed a "patchy" phenotype; i.e., a large region of the embryo undergoes the MBT at the appropriate time, while another one undergoes an extra cell division. It is an open issue whether patchiness is due to inhomogeneities in the activity of Cdk1 and/or other cell cycle regulators or results from an aborted wave that fails to spread across the entire embryo (28).

To discriminate the two scenarios above, we used compound chromosomes to alter the DNA content of embryos (28) and generated a variety of mitotic phenotypes. Embryos lacking a copy of chromosome 2 feature the following dynamics: A fraction of them arrests at cycle 14 as the wild type, a fraction undergoes an extra mitosis, and a fraction shows the patchy behavior defined above (Fig. 8). Inspection of the embryos where the Cdk1 activity increases slowly during cell cycle 14 reveals that Cdk1 eventually relaxes back to a fully inactive state (Fig. 8 *F* and *J*). Conversely, Cdk1 can initiate a mitotic wave (Fig. 8 *G*, *H*, *K*, and *L*) if its rate of activation is fast enough. In sum, depending on the rate of Cdk1 activation, waves spread and initiate mitosis throughout the embryo (Fig. 8*G*) or slow down and die out, causing the patchy phenotype (Fig. 8*H*).

We then modified our mathematical model as follows. First, we used the fact that the S-phase rate of Cdk1 activation (which reflects the Chk1 level) is higher in embryos that lack one copy of

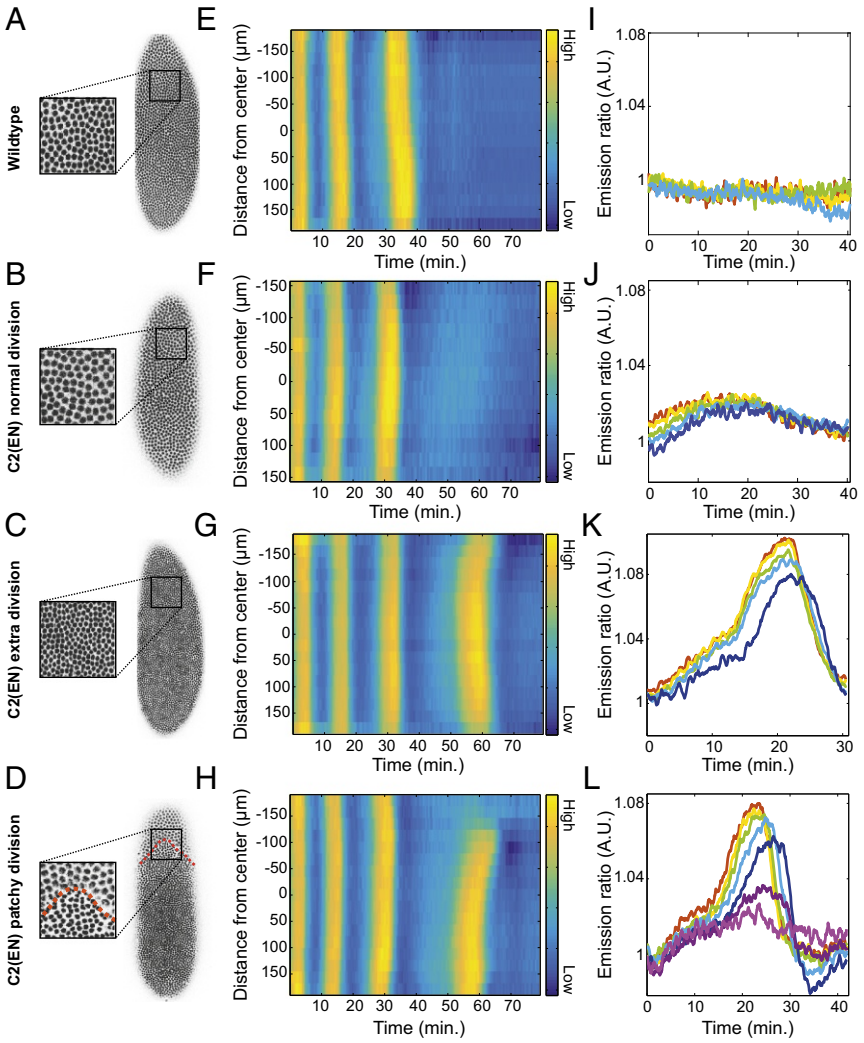

Fig. 8. Inhibition of Cdk1 waves at the maternal-to-zygotic transition. (*A–D*) Nuclear density for wild-type embryo (*A*) and three embryos with reduced DNA content (*B–D*), obtained from a cross between wild-type females and *C*(2)*EN* males. These embryos show three different phenotypes: normal nuclear density, uniformly increased nuclear density due to an extra cell division, and nonuniform nuclear density due to a patchy extra division. The zoom-in in *D* highlights the sharp boundary between the region that underwent the extra division and the one that did not. (*E–H*) Heat maps of Cdk1 activity from cell cycle 11 to the maternal-to-zygotic transition for the wild-type embryo (*E*) and the three embryos with reduced DNA content (*F–H*). In cell cycle 14, the patchy embryo shows a wave of Cdk1 activity, which is unable to propagate throughout the entire embryo (*H*), resulting in the differences in nuclear density observed in *D*. (*I–L*) Plots of Cdk1 activity at cell cycle 14 for different regions of the embryos for the wild type (*I*) and for the three embryos with reduced DNA content (*J–L*). In cell cycle 14 of the patchy embryo, Cdk1 activity dampens as it propagates (*L*) until it rapidly drops and becomes unable to initiate mitosis across the entire embryo. A small dampening is also observed in embryos undergoing an extra division (*K*), but the effect is small and mitosis is initiated and completed across the entire embryo. For further details, see Fig. S8.

chromosome 2 compared with wild type (21). To take that into account, we simulated the behavior of embryos at cell cycle 14 by using values of Chk1 that still allow slow activation of Cdk1, as observed in experiments (Fig. 8 *J–L*). Second, we included degradation of the Cdc25 phosphatase Twine, which is known to control the cell cycle pause at the MBT (29, 30). Indeed, imaging of embryos expressing Twine tagged with GFP shows that, as in wild type, the protein is degraded rapidly during cell cycle 14 of embryos with one copy of chromosome 2. The modified model reproduces the patchy phenotype (Fig. S8).

The above results suggest the following scenario. At early times of the cell cycle 14, when high levels of Twine are still present, the Cdk1 dynamics proceed as in wild-type cell cycle 13 embryos, and a transient metastability is observed. Eventually, the system either becomes monostable or displays a very small barrier between the stable and the metastable states of high/low Cdk1 activity, respectively. A wave is then initiated, yet Twine decays to low levels, which leads to a switch in stability. In other words, the high state of Cdk1 activity becomes metastable and the low state becomes stable, so that the wave stops. These results support the aborted-wave scenario.

Discussion

We have shown that Cdk1 waves in wild-type *Drosophila* embryos hinge on time-dependent effects in the reaction dynamics of the feedback loops among Cdk1, Wee1, Cdc25, and Chk1. During the S phase of the cell cycle, time-dependent effects become dominant and produce the upward sweep of the Cdk1 levels of activity visible in Fig. 1*A*. The sweep is roughly uniform in space and therefore preserves the Cdk1 spatial gradients. Since gradients swept upward reach prescribed levels with delays that vary roughly linearly in space, a wave-like spreading is produced, which accounts for experimental observations in wild-type *Drosophila* embryos.

The above mechanism differs fundamentally from the coupling of bistability and diffusion proposed for *Xenopus* extracts (12) and has a major impact upon the waves' speed u and its dependency on physical parameters. For instance, Eq. **11** predicts that u should be inversely proportional to the spatial gradients g of Cdk1. This is intuitive since the shallower is the profile of Cdk1 levels of activation, the more extended is the spatial region that will cross a threshold level as the Cdk1 profile is swept upward. Two consequences follow: (*i*) Since the gradients are proportional to the strength of the fluctuations, the speed u increases as the level of noise in the dynamics reduces, and (*ii*) since gradients increase with the strength of the reaction terms, u decreases as the strength of the feedback loops increases. Both dependencies differ markedly from the behavior of bistable waves. Similarly, strong differences are found for the dependency on the S-phase Cdk1 activation rate k_S and the Cdk1 molecular diffusivity D. In particular, our predictions for the k_S dependency explain previous empirical experimental observations (figure 2 in ref. 21).

During the phase of uniform growth that leads to sweep waves, spatial points are largely decoupled, as in kinematic phase waves. However, the spatial Cdk1 gradients (and the consequent wave-like spreading) are generated dynamically by the combined action of diffusion, noise, and feedback loops. Therefore, the insertion of a physical barrier between two embryonic regions prevents the buildup of a gradient across them. It follows that the two separated regions will be decoupled and asynchronous, as observed in ligation experiments (21, 27) and demonstrated for the developmental model Eq. **1** by simulations reported in Fig. S2*H*.

Our work was motivated and enabled by the in vivo measurements of the Cdk1 dynamics with high spatiotemporal precision (21). It would be important to develop similar experimental tools for *Xenopus*, to ascertain the nature of its Cdk1 and surface contraction waves. In vitro experiments using egg extracts show a wide range of wave speeds in *Xenopus laevis* and a substantial slowdown across the cycles (figure 2 in ref. 12), making it plausible that time-dependent mechanisms play a fundamental role.

We conclude with the possible selective advantages of sweep vs. bistable waves. Notably, the former are faster and take place for larger values of the Cdk1 activation rate k_S during the S phase; i.e., sweep waves are associated with a faster drive of the cell cycle. Proper morphogenesis and the risk of predation impose selective pressure for early embryogenesis to proceed in a rapid and coordinated manner. We speculate that sweep waves have evolved to ensure that cell cycles in the *Drosophila* syncytium are synchronized and completed in minutes rather than several tens of minutes, which the reduced drive of the S phase and slower bistable waves would entail. The biological importance of speed suggests that mechanisms presented here should be relevant to other developmental processes, which can similarly benefit from recent progress on in vivo optical methods coupled with quantitative analyses.

Materials and Methods

Numerical Simulations. Partial differential stochastic Eqs. **1** and **2** were simulated in MATLAB and in C, using standard finite-difference methods. The speed of the waves u was measured by determining the times at which the simulated field crosses a given threshold level as a function of space. The deterministic speed of bistable waves was computed by solving the differential Eq. **5** for initially high u and decreasing its value until the simulated point mass lands asymptotically on the metastable peak of the inverted potential $-V$. The speed of noisy bistable waves as in Fig. 2*G* was computed by evolving an initial condition with a region of the field set at the value of the stable fixed point and the rest at the metastable value (with a sharp transition in between).

Deviations to the Adiabatic Regime. We consider the equation $d\phi(t)/dt = F(\phi, t)$, with F as in Eq. **3**. This describes the deterministic growth at a point in a linear gradient and also the growth of the average for Eq. **2** in the limit of small noise, so that $\langle F(\phi, t)\rangle \simeq F(\langle\phi\rangle, t)$. When β is small and the derivative $dF/d\phi$ at the fixed point ϕ_0 is large and negative, i.e., fluctuations are small, the solution is $\langle\phi\rangle = \phi_0(\zeta) - \beta\frac{d\phi_0/d\zeta}{|F'(\phi_0,\zeta)|}$, where $F' = \partial F/\partial\phi$ and $\zeta \equiv \beta t$. By using $F(\phi_0(\zeta), \zeta) = 0$ and the linearity of F in ζ, we obtain $F'(\phi_0, \zeta)(d\phi_0/d\zeta) = -1$, whence $\langle\phi\rangle \simeq \phi_0(\zeta) - \beta(d\phi_0/d\zeta)^2$. The correction is negative; i.e., the field is delayed with respect to ϕ_0, as expected. The correction for small β is initially minor, yet it eventually diverges to $\propto (F^* - \zeta)^{-1}$ as ζ approaches F^*.

Slowly Varying Potential. We consider a slowly varying F in Eq. **2**, i.e., small β, with the aim of determining the dependency of the speed of bistable waves on the drive β.

The ratio between the height of the metastable barrier (Figs. 2*B* and 4*B*) and the amplitude of fluctuations of ϕ is $(\phi_1 - \phi_0)/\sqrt{C(0)}$. As $\zeta = \beta t$ grows, the numerator reduces and the denominator increases (Eq. **7**), which eventually leads to a jump above the metastable barrier. Jumps typically occur at values of ζ such that the rate of transition across the metastable barrier multiplied by the time spent at the level ζ is of order unity. For the latter, since $d\phi_0/dt = \beta d\phi_0/d\zeta$, the time spent at the level ζ is inversely proportional to β. For the former, a jump requires that the maximum of ϕ over the size L of the system passes the threshold imposed by the metastable barrier. Strong excursions are the subject of extreme values theory (31). For Uhlenbeck–Ornstein processes (as in Eq. **7**), relevant results are fully reviewed in *The Probability of Overcoming the Metastable Barrier: Scaling of the Wave Speed in Slowly Varying Potentials*. The upshot is that the exponentially dominant term (apart from dimensional prefactors) for the rate of transition above the metastable barrier is

$$P_{\text{thr}} \propto \exp\left[-\frac{(\phi_1 - \phi_0)^2}{2C(0)}\right], \qquad [12]$$

i.e., the Gaussian factor that gives the probability for ϕ at a single point to pass the metastable barrier.

In summary, the dominant dependency on β for the triggering of bistable waves is determined by the scaling relation $P_{\text{thr}} \propto \beta$. By using the expressions of $\phi_1 - \phi_0$ and $C(0)$ in Eq. **7**, we conclude that

$$F^* - \zeta_{\text{tr}} \propto (-\log\beta)^{4/5}; \quad u^* - u \propto (-\log\beta)^{2/5}, \qquad [13]$$

where ζ_{tr} is the typical value of ζ when bistable waves are triggered, their speed is u, and u^* is their maximum speed (Fig. 4*D*) at the loss of bistability (for $\zeta = F^*$ in Eq. **3**).

The weak dependency on β corresponds to the region of small βs in Fig. 5*A* and is rationalized as follows. As β reduces, the growth of ϕ takes longer, and rare jumps that trigger bistable waves occur with higher chance. However, since the growth of ϕ is roughly linear in time, while the probability of overcoming the metastable barrier is exponentially small in its height, altering the rate of growth has logarithmically weak effects. The specific 2/5 prediction in Eq. **13** is confirmed by extensive numerical simulations (Fig. 5*A*, *Inset*).

More Details on the Sweep Phase II. Close to its minimum ϕ^*, the force in Eq. **3** is well approximated by its quadratic expansion Eq. **8**. We consider the equation $\beta d\Phi/dz = F_{quadr}(\Phi)$, where $\Phi \equiv \phi - \phi^*$, $z \equiv \zeta - \zeta^*$, and $F_{quadr}(\Phi) = \gamma\Phi^2 + z + \zeta^* - F^*$ with γ defined in Eq. **8**. The equation describes the deterministic growth for a linearly varying region where diffusion can be neglected. It also describes the dynamics of the average $\langle\phi\rangle - \phi^*$ when fluctuations are small, so that $\langle F_{quadr}(\phi)\rangle \simeq F_{quadr}(\langle\phi\rangle)$. The validity of the small-noise approximation is confirmed by numerical simulations in Fig. S6*B* and ultimately traces back to the fact that strong fluctuations due to regions of the field coexisting in different (metastable vs. stable) phases (Fig. 5*C*) are not present for fast drive.

It is verified that the equation $\beta d\Phi/dz = F_{quadr}(\Phi)$ has a scale-invariant form if Φ^2, z, and $\zeta^* - F^*$ are rescaled by $\beta^{2/3}$, as confirmed by numerical simulations in Fig. S6. In the window around ϕ^* where the term quadratic in Φ is negligible, the integration of $\beta d\Phi/dz = z + \zeta^* - F^*$ with $\Phi = 0$ at $z = 0$ yields Eq. **9**.

Finally, we derive the scaling of the gradients at the entry into phase II. Fluctuations $\phi - \langle\phi\rangle$ obey Eq. **6**, with the fixed point ϕ_0 replaced by the mean $\langle\phi\rangle$, and the relaxation time $\tau^{-1} \simeq 2\gamma(\phi^* - \langle\phi\rangle)$, which is obtained by taking the derivative of the above quadratic approximation F_{quadr} at $\langle\phi\rangle - \phi^*$. The validity of the linearization is granted by the above arguments. Treating τ as fixed is meaningful as long as τ does not change significantly over the relaxation time itself; i.e., $d\tau/dt \lesssim 1$. It is verified that

this condition is satisfied; i.e., there is no factor growing with β for the $\beta^{2/3}$ scalings of $(\phi^* - \langle\phi\rangle)^2$, $\zeta - \zeta^*$, and $\zeta^* - F^*$ found above. The variance and the correlation length of the fluctuations are finally calculated as in Eq. **7**, which yields the formulas in the main text.

Stocks. Stocks were generated using standard methods. The *cyclin B* and *cyclin A* heterozygous embryos had the genotype *w; cycB*^{2}*/CDK1 FRET His2Av-mRFP; cycA*^{C8}*/CDK1 FRET His2Av-mRFP*. The mitotic switch mutants were generated as detailed in ref. 21. To generate embryos with different DNA content, we used homo compound chromosomes *C(2)EN*, in which both copies of chromosome 2 are fused together. To that end, we crossed *w; CDK1 FRET; His2Av-mRFP* females to *C(2)EN* males.

Imaging. Embryos were collected on apple juice agar plates after 0–2 h at 25 °C. Following collection, embryos were dechorionated with 50% bleach for 1 min and rinsed with water. Embryos were mounted in Halocarbon oil 27 on a slide with an air-permeable membrane on one side and a glass coverslip on the other. Imaging experiments were performed with an upright Leica SP8 confocal microscope, a 20×/0.75 numerical aperture oil-immersion objective, an argon ion laser, and a 561-nm diode laser. We acquired images (800 × 300 pixels) with a frame rate of 1/2.89 s.

Data and Image Analysis. Cdk1 FRET curves were computed by the fluorescence intensity ratio of YFP over CFP signals, averaged over vertical slices of a width of 22.4μm. The speed of Cdk1 waves was measured by the computational procedure described in ref. 21.

ACKNOWLEDGMENTS. The authors acknowledge discussions with A. Celani, E. D. Siggia, and E. F. Wieschaus. This work was partly supported by a HHMI International Student Research Fellowship and a Schumblerger Faculty for the Future Fellowship (to V.E.D.) and by NIH Grants R00-HD074670 and R01-GM122936 (to S.D.T.).

1. O'Farrell PH (2015).Growing an embryo from a single cell: A hurdle in animal life. *Cold Spring Harb Perspect Biol* 7:a019042.
2. O'Farrell PH, Stumpff J, Su TT (2004) Embryonic cleavage cycles: How is a mouse like a fly? *Curr Biol* 14:R35–R45.
3. Tyson JJ, Keener JP (1988) Singular perturbation theory of spiral waves in excitable media. *Phys D* 32:327–361.
4. van Saarloos W (1998) Three basic issues concerning interface dynamics in nonequilibrium pattern. *Phys Rep* 301:9–43.
5. Ben-Jacob E, Brand H, Dee G, Kramer L, Langer JS (1985) Pattern propagation in nonlinear dissipative systems. *Physica D* 14:348–364.
6. Mikhailov AS, Schimansky-Geier L, Ebeling W (1983) Stochastic motion of the propagating front in bistable media. *Phys Lett* 96:453–456.
7. Brunet E, Derrida B (1997) Shift in the velocity of a front due to a cutoff. *Phys Rev E* 56:2597–2604.
8. Lindner B, Garcıa-Ojalvo J, Neiman A, Schimansky-Geier L (2004) Effects of noise in excitable systems. *Phys Rep* 392:321–424.
9. Panja D (2004) Effects of fluctuations on propagating fronts. *Phys Rep* 393:87–174.
10. Montroll EW (1972) *Statistical Mechanics*, eds Rice SA, Freed KF, Light JC (Univ of Chicago Press, Chicago), p 69.
11. Nitzan A, Ortoleva P, Ross J. (1974) Nucleation in systems with multiple stationary states. *Faraday Symp Chem Soc* 9:241–253.
12. Chang JB, Ferrell JE, Jr (2013) Mitotic trigger waves and the spatial coordination of the *Xenopus* cell cycle. *Nature* 500:603–607.
13. Novak B, Tyson JJ (1993) Numerical analysis of a comprehensive model of M-phase control in *Xenopus* oocyte extracts and intact embryos. *J Cell Sci* 106:1153–1168.
14. Gelens L, Huang KC, Ferrell JE, Jr (2015) How does the *Xenopus laevis* embryonic cell cycle avoid spatial chaos? *Cell Rep* 12:892–900.
15. McIsaac RS, Huang KC, Sengupta A, Wingreen NS (2011) Does the potential for chaos constrain the embryonic cell-cycle oscillator? *PLoS Comput Biol* 7:e1002109.
16. Koke C, Kanesaki T, Grosshans J, Schwarz US, Dunlop CM (2014) A computational model of nuclear self-organisation in syncytial embryos. *J Theor Biol* 359:92–100.
17. Rabinowitz M (1941) Studies on the cytology and early embryology of the egg of *Drosophila* melanogaster. *J Morphol* 69:1–49.
18. Ferree PL, Deneke VE, Di Talia S (2016) Measuring time during early embryonic development. *Semin Cell Dev Biol* 55:80–88.
19. Ferrell JA, O'Farrell PH (2014) From egg to gastrula: How the cell cycle is remodeled during the *Drosophila* mid-blastula transition. *Annu Rev Genet* 48:269–294.
20. Idema T, et al. (2013) The syncytial *Drosophila* embryo as a mechanically excitable medium. *PLoS One* 8:e77216.
21. Deneke VE, Melbinger A, Vergassola M, Di Talia S (2016) Waves of Cdk1 activity in S phase synchronize the cell cycle in *Drosophila* embryos. *Dev Cell* 38:399–412.
22. Morgan DO (2007) *The Cell Cycle: Principles of Control* (New Science Press, Sunderland, MA).
23. Lindqvist A, Rodriguez-Bravo V, Medema RH (2009) The decision to enter mitosis: Feedback and redundancy in the mitotic entry network. *J Cell Biol* 185:193–202.
24. Gillespie DT (2007) Stochastic simulation of chemical kinetics. *Annu Rev Phys Chem* 58:35–55.
25. Newport J, Kirschner MW (1982) A major developmental transition in early *Xenopus* embryos: I. Characterization and timing of cellular changes at the midblastula stage. *Cell* 30:675–686.
26. Newport J, Kirschner MW (1982) A major developmental transition in early *Xenopus* embryos: II. Control of the onset of transcription. *Cell* 30:687–696.
27. Edgar BA, Kiehle CP, Schubiger G (1986) Cell cycle control by the nucleo-cytoplasmic ratio in early *Drosophila* development. *Cell* 44:365–372.
28. Lu X, Li JM, Elemento O, Tavazoie S, Wieschaus EF (2009) Coupling of zygotic transcription to mitotic control at the *Drosophila* mid-blastula transition. *Development* 136:2101–2110.
29. Di Talia S, et al. (2013) Posttranslational control of Cdc25 degradation terminates *Drosophila* early cell-cycle program. *Curr Biol* 23:127–132.
30. Farrell JA, O'Farrell PH (2013) Mechanism and regulation of Cdc25/Twine protein destruction in embryonic cell-cycle remodeling. *Curr Biol* 23:118–126.
31. Kotz S, Nadarajah S (2000) *Extreme Value Distributions: Theory and Applications* (Imperial College Press, London), 1st Ed.